SciEn
Journal of Engineering Advancements Vol. 07(02) 2026, pp 81-88 https://doi.org/10.38032/jea.2026.02.005

# CFD-Based Numerical Analysis of Aerodynamic Performance for Different NACA Airfoils

*Muhammad Shahryar*[*1,2], *Muhammad Fahadyar*[2]

[1]School of Energy and Power Engineering, Xi'an Jiaotong University, Xi'an, Shaanxi, People's Republic of China.
[2]Department of Mechanical Engineering, University of Engineering and Technology, Lahore, 54890, Pakistan

Received: November 23, 2025, Revised: May 23, 2026, Accepted: June 07, 2026, Available Online: July 09, 2026

## ABSTRACT

Aeronautical engineering relies critically on the optimization of aerodynamic airfoil shapes, the precise configuration of which significantly influences aircraft efficiency. Consequently, comprehensive research aimed at improving these designs is essential for advancing aerospace innovation. In this study, computational fluid dynamics (CFD) is employed to numerically analyze the flow behavior over distinct NACA airfoil profiles under various angles of attack, encompassing both low-speed and high-speed regimes. The primary objective is to identify viable pathways for enhancing wing-section aerodynamics. Initial analysis confirms that the angle of attack exerts a substantial influence on the lift-to-drag ratio, establishing it as a key performance metric. The validity of the numerical methodology is demonstrated by a clear correlation observed between the CFD predictions and established experimental data, thereby affirming its capability for accurate simulation of aerodynamic phenomena. Results from both the numerical and experimental investigations consistently indicate that the asymmetric airfoil profile attains a superior lift-to-drag ratio compared to its symmetric counterpart.

Keywords: NACA Airfoil, Angle of Attack, Aerodynamic Performance, Computational Fluid Dynamics (CFD).

## 1 Introduction

An airfoil is a streamlined structure that, when moving through a fluid, generates an aerodynamic force resulting from surface pressure and shear stress. This force can be resolved into two components: lift, which acts perpendicular to the direction of motion, and drag, which acts parallel to it. The lift force is primarily governed by the airfoil's surface geometry and its angle of attack. In contrast, the drag force is determined largely by the body's surface characteristics and the properties of the surrounding fluid. The ability to design an effective airfoil configuration is crucial to meeting the technical and economic objectives of modern aircraft design, as it enables greater payload capacity, higher speeds, and lower energy consumption. Aerodynamic performance is commonly quantified by the lift-to-drag ratio, making the optimization of this parameter a central focus in the development of next-generation aircraft.

While fluid resistance (drag) is commonly understood as the force opposing an object's motion, certain streamlined profiles can generate a significantly greater force perpendicular to the flow direction, known as lift [1] Computational Fluid Dynamics (CFD) has become an indispensable tool in modern airfoil research. Compared with conventional wind-tunnel testing, CFD provides a faster, more efficient alternative while delivering results of comparable accuracy and reliability. For instance, Kanimozhi [2] validated CFD-derived lift and drag coefficients against experimental wind-tunnel data, demonstrating strong agreement. Moreover, numerous studies have evaluated the performance of specific CFD models, further establishing confidence in simulation outcomes. GÖRGÜLÜ et al. [3] employed CFD to identify the optimal angle of attack (AOA) for a NACA 0009 airfoil, while Chumbre et al. [4] compared the lift-to-drag ratios of five distinct NACA profiles using CFD-based analysis. Using Computational Fluid Dynamics (CFD), Peng et al. [5] investigated the combined lift and drag characteristics of an airfoil. The aerodynamic properties of NACA-series airfoils can be derived from their four-digit designations via mathematical relations. These parameters allow for efficient calculation of key performance metrics and generation of the corresponding cross-sectional geometry. For instance, the NACA 4412 profile can be directly constructed and analyzed based on its designated numerical code [6],[7].

To be effectively applied in wind turbines and aircraft, an airfoil must achieve optimal aerodynamic efficiency, which entails generating high lift while minimizing drag to ensure enhanced performance and energy economy [8]. In an experimental study, Islam Rubel et al. [9] analyzed the NACA 0015 airfoil in a low-speed wind tunnel, measuring aerodynamic forces at 2° increments from 0° to 18°. The results confirmed the expected strong dependence of the lift coefficient on the angle of attack. Other research has examined numerical modeling parameters; for example, Aqilah Aqilah et al [10] demonstrated that mesh quality significantly influences CFD simulation outcomes.

Although airfoil aerodynamics is a well-established field, systematic investigation of airfoil design remains incomplete, offering multiple avenues for further exploration. Wolfe and Ochs [11] compared CFD-predicted and experimentally measured aerodynamic coefficients for the NACA 0021 airfoil. They concluded that accurate numerical simulation of wind turbine airfoils requires further advances in two key CFD areas: transition prediction and turbulence modeling. This observation was later supported by Langtry et al. [12], who applied a transition-sensitive model to predict the performance of 2D and 3D wind turbine airfoils. Their results showed close agreement with experimental data, validating the model's suitability for capturing the aerodynamic behavior of such airfoils.

*Corresponding Author Email Address: mshaheryar857@gmail.com

This study presents a comprehensive numerical and experimental investigation of the aerodynamic performance of multiple airfoil profiles. It systematically examines the critical interaction between camber—comparing symmetrical and asymmetrical designs—and trailing-edge geometry, specifically sharp versus square configurations, across a broad range of angles of attack. The primary objective is to quantify the influence of these fundamental design parameters on key performance indicators, including lift and drag coefficients, lift-to-drag ratio, and stall characteristics. Through comparative analysis under consistent flow conditions, the work aims to clarify the distinct advantages and trade-offs inherent to each configuration. The results are expected to provide quantitative insights that can guide the selection and optimization of airfoil shapes for specific aerodynamic applications, where performance requirements must be balanced with structural and operational constraints.

### 1.1 Airfoil Geometry Definition

An airfoil refers to the characteristic cross-sectional shape of a wing, a blade, or any other aerodynamic body. A classic airfoil profile features a curved upper surface and a comparatively flatter (or similarly curved) lower surface. Symmetrical and asymmetrical airfoils differ fundamentally in their geometry, as illustrated in Fig. 1 and Fig. 2.

The aerodynamic performance of an airfoil is governed primarily by its geometric parameters [13], which include the leading edge at the front, the trailing edge at the rear, and the chord line—a straight line connecting the two edges. The mean camber line defines the profile's curvature, while the angle of attack denotes the inclination of the chord line relative to the oncoming freestream direction. For a finite wing, the aspect ratio, defined as the wing span divided by the average chord length, serves as a key design parameter.

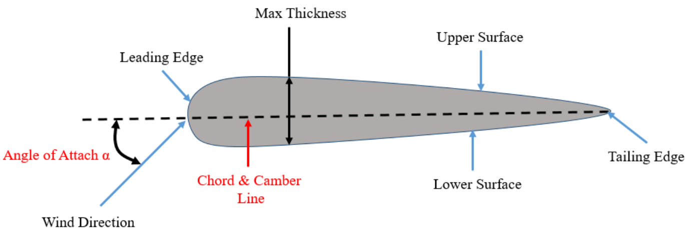

Fig. 1 Symmetric Airfoil

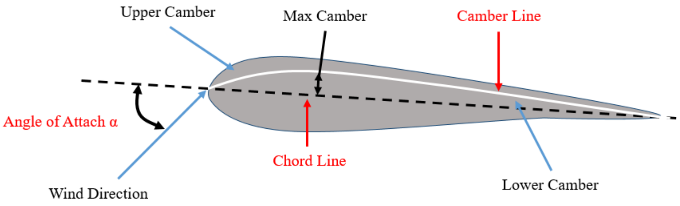

Fig. 2 Asymmetric Airfoil

## 2 Modelling and Simulation Method

### 2.1 Analytical Approach

This section outlines the methodology and analytical calculation employed in this simulation. The formulation for the simulation is based on the continuity equation, among other governing equations. Our system is pressure-based solver therefore we don't need energy equation.

Continuity equation:

$$\frac{\partial(\rho u)}{\partial x} + \frac{\partial(\rho v)}{\partial y} = 0 \tag{1}$$

And Navier-Strokes equations:

X-momentum:

$$\frac{\partial(\rho u^2)}{\partial x} + \frac{\partial(\rho uv)}{\partial y} = -\frac{\partial p}{\partial x} + (\upsilon + \upsilon_T)\left(\frac{\partial^2 u}{\partial x^2} + \frac{\partial^2 u}{\partial y^2}\right) \tag{2}$$

Y-momentum:

$$\frac{\partial(\rho uv)}{\partial x} + \frac{\partial(\rho v^2)}{\partial y} = -\frac{\partial p}{\partial x} + (\upsilon + \upsilon_T)\left(\frac{\partial^2 v}{\partial x^2} + \frac{\partial^2 v}{\partial y^2}\right) - g \tag{3}$$

Reynold and Mach number:

$$Re = \frac{\rho v L}{\mu} \tag{4}$$

$$\text{Mach Number} = \frac{Velocity\ of\ fluid}{Velocity\ of\ sound}$$

Here, u & v represents the velocity components, p is the pressure, $\upsilon$ is the kinematic viscosity, $\upsilon_T$ is the eddy viscosity, which is find by the k-ω model Wilcox, [14] , ρ is the density, $F_d$ is the drag force, $F_l$ is the lift force, $u'$ is the fluid relative velocity, A is the perpendicular area to the direction of the fluid, $V_\infty$ is the free-stream velocity of the fluid, $p_\infty$ is the free-stream static pressure, $p$ is the local static pressure and $\rho_\infty$ is the free-stream density of the fluid. An airfoil's performance is primarily measured by how much lift it generates (lift coefficient) versus how much drag it creates (drag coefficient). Here, the Coefficient are defined as

Drag, Lift and Pressure Coefficient:

$$C_d = \frac{2F_d}{\rho u'^2 A} \tag{5}$$

$$C_l = \frac{2F_l}{\rho u'^2 A} \tag{6}$$

$$C_p = \frac{p - p_\infty}{\frac{1}{2}\rho_\infty {V_\infty}^2} \tag{7}$$

The generation of lift is inherently accompanied by the production of drag, as illustrated in Fig. 3. Consequently, the lift-to-drag ratio, denoted as $C_l$/Cd, serves as the fundamental metric of an airfoil's aerodynamic efficiency, quantifying its capacity to balance these opposing forces. This ratio, therefore, provides a critical criterion for evaluating and comparing the performance of different airfoil designs.

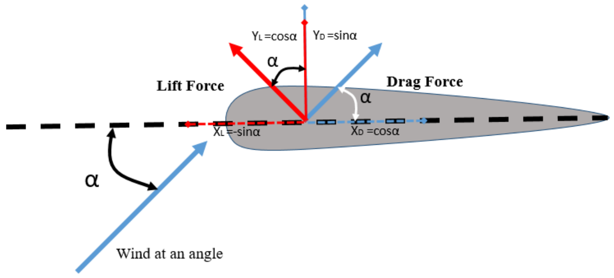

Fig. 3 Resolve the Component into Lift and Drag Forces

### 2.2 Numerical Approach

This analysis utilizes a database of airfoils, primarily comprising symmetrical and non-symmetrical designs from the NACA series, sourced from established public repositories. To enable a comparative study, two distinct airfoils were selected from this database; their specifications are provided in Table 1.

Table 1 Specification of Airfoil

| | **NACA Symmetric Airfoil** | **NACA Asymmetric Airfoil** |
|---|---|---|
| Max Chamber (%) | 0 | 4 |
| Max Chamber Position (%) | 0 | 40 |
| Thickness (%) | 12 | 12 |
| Number of points | 81 | 81 |
| Chord Length (m) | 1 | 1 |

The preprocessing phase forms the foundation of the computational fluid dynamics (CFD) workflow and requires high precision to ensure accurate simulation results. In this study, the airfoil geometries were constructed using computer-aided design (CAD) software, specifically ANSYS Design Modeler and Space Claim. The x- and y-coordinates for the selected airfoils were obtained from a public airfoil database and imported directly into the CAD environment to generate the precise profiles needed for simulation. To investigate the effect of trailing-edge geometry on flow separation—specifically sharp versus square configurations, as illustrated in Fig. 4 this design variation was applied to the airfoil series.

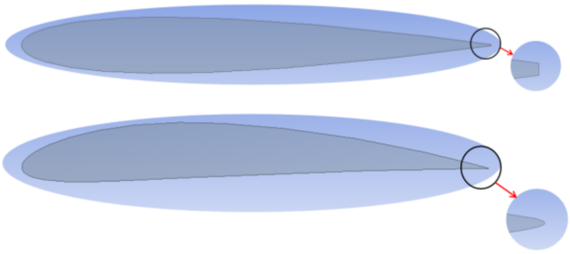

Fig. 4 Airfoil with Sharp & Square TE

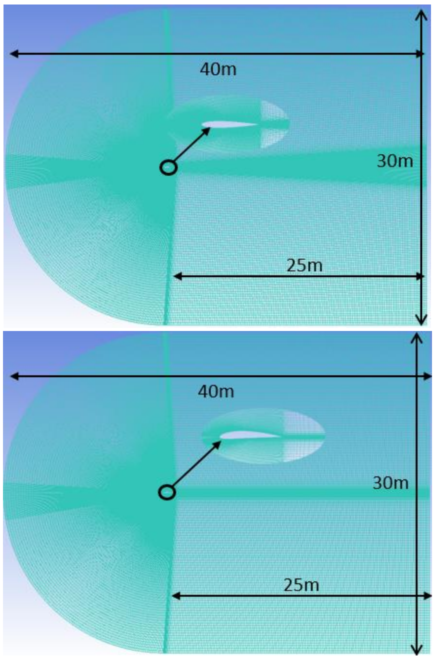

Fig. 5 ICEM Meshing

In this study, the airfoil geometries were discretized using ANSYS ICEM CFD to generate a high-quality hybrid mesh, as illustrated in Fig. 5. The computational domain extended 15 chord lengths (15c) upstream of the airfoil leading edge and 25 chord lengths (25c) downstream of the trailing edge. A C-type topology was applied around each airfoil to ensure smooth cell distribution, particularly in the wake region. The domain dimensions were selected to minimize boundary interference, and the mesh was refined with near-wall inflation layers to resolve the boundary layer accurately, maintaining a suitable $y^+$ value for the turbulence model. Mesh density was gradually coarsened away from the airfoil to optimize computational efficiency. Grid-independence was assessed by evaluating the simulation results for different mesh densities, as summarized in Table 2. The results obtained with 94,120 elements showed negligible deviation (less than 5%) from those with 110,254 elements. Based on this minimal variation and the lower computational cost, the mesh with 94,120 elements was selected for all subsequent simulations. The same grid-independence verification process was applied to each airfoil geometry.

Table 2 Changes of different aerodynamic coefficients with the number of grid elements.

| Grid # | Number of elements | $C_d$ | $C_l$ |
|---|---|---|---|
| 1 | 82610 | 0.007861 | 3.149E-05 |
| 2 | 85248 | 0.008452 | 3.9808E-05 |
| 3 | 94120 | 0.009061 | 4.7178E-05 |
| 4 | 110254 | 0.009125 | 5.1038E-05 |

Mesh quality metrics—including orthogonality, skewness, and aspect ratio—were rigorously controlled to ensure numerical stability and solution convergence, as detailed in Table 3. The orthogonal quality for all cells was maintained above 0.01, and the minimum cell volume was ensured to be positive.

Table 3 Mesh Quality

| Case # | No of Nodes | Minimum Volume | Min Orthogonal Quality | Max Aspect Ratio | Quality 3x3x3 |
|---|---|---|---|---|---|
| Symmetric Close | 94120 | 4.933058e-08 | 1.90316e-01 | 3.07007e+03 | 0.881 |
| Symmetric Open | 95280 | 4.620307e-08 | 1.71472e-01 | 4.13661e+03 | 0.778 |
| Asymmetric Close | 94120 | 3.820928e-08 | 9.75726e-02 | 3.06744e+03 | 0.876 |
| Asymmetric Open | 103920 | 3.569428e-08 | 8.69733e-02 | 3.41648e+03 | 0.828 |

The numerical solution of the governing fluid flow equations requires the specification of appropriate boundary conditions to define the problem at the domain limits. The accurate imposition of these conditions is critical, as errors or omissions can lead to non-physical results and convergence issues. For the present simulation, the applied boundary conditions include inlet, outlet, wall, and interface types are shown in Table 4. The k-omega shear-stress transport (SST) model was employed in this study due to its superior accuracy for flows involving adverse pressure gradients and boundary-layer separation, conditions prevalent in airfoil aerodynamics, compared to the standard k-epsilon model.

Table 4 Design Parameters

| | |
|---|---|
| Reynolds number | 3 million |
| Chord length | 1 m |
| Density | 1.225 |
| Viscosity | 1.79E-05 |
| Velocity | 43.822 |
| Mach Number | 0.12889 |
| Gauge Pressure | 0 Pa |
| Operating Pressure | 101325 Pa |
| Shear Condition | No Slip Condition |
| Model | K-omega (SST) |
| Turbulence Intensity (%) | 0.1 |
| Turbulent Length Scale (m) | 0.3 |
| Algorithm Scheme | Coupled |
| Residual Value | 1e-06 |

Aerodynamic performance is critically governed by the behavior of the boundary layer the thin region of viscous flow adjacent to a surface. For the low Mach number (Ma < 0.3) conditions considered in this study, the flow is incompressible, and the state of the boundary layer (laminar or turbulent) is determined by the Reynolds number. A key phenomenon is boundary layer separation, which occurs under adverse pressure gradients and results in a substantial increase in drag. A principal objective of aerodynamic design is therefore to employ flow control strategies that delay separation and maintain attached flow.

## 3 Results and Discussions

This study conducts a detailed computational fluid dynamics (CFD) analysis of the aerodynamic performance of multiple NACA-series airfoils, each possessing a chord length of one meter. The investigation specifically examines the influence of two primary geometric variables: trailing-edge configuration (sharp versus square) and profile camber (symmetric versus asymmetric). By systematically varying the angle of attack, the simulations capture the progression of flow phenomena from the linear aerodynamic regime through stall onset and into the post-stall condition. Results are presented in the form of force-coefficient polars and detailed flow-field visualizations, which together elucidate the interplay between geometric design, surface pressure distribution, boundary-layer development, and overall aerodynamic efficiency.

### 3.1 Quantitative Performance Trends and Physical Interpretation

### 3.1.1 Lift and Drag Coefficient Correlation

As presented in Fig. 6, the numerical predictions for lift coefficient ($C_l$) and drag coefficient ($C𝑑$) exhibit strong qualitative agreement with established experimental data from the NACA database and prior literature [7],[8]. The linear rise in $C_l$ with increasing angle of attack (AOA) in the pre-stall regime (typically 0° to ~10°) is a direct consequence of enhanced flow turning. This strengthens the leading-edge suction peak on the upper surface, thereby amplifying the pressure differential between the upper and lower surfaces. The concomitant increase in $C𝑑$ is not merely parasitic but is physically comprised of two primary components: pressure drag, which escalates as the effective frontal area presented to the flow increases with AOA, and viscous skin-friction drag, which grows due to the lengthening of the surface-tangential flow path and increased shear stress.

### 3.1.2 Lift-to-Drag Ratio: Optimal Performance and the Onset of Stall

The lift-to-drag ratio ($C_l/C𝑑$), shown in Fig. 7, serves as the definitive metric of aerodynamic efficiency. The simulation successfully replicates the characteristic trend: a sharp initial increase, a distinct peak value between 70 and 80 occurring at 8°–10° AOA, followed by a progressive decline. This peak represents the optimal operational point where the airfoil generates the maximum useful lift per unit of drag penalty. The subsequent decay signals the growing dominance of adverse pressure gradients, which first initiate boundary-layer separation near the trailing edge. The consistent computational underestimation of $C_l/C𝑑$, particularly pronounced at AOAs exceeding 14°, is analytically attributed to inherent limitations of the RANS-based k-ω SST turbulence model in fully resolving the complex, three-dimensional, and inherently unsteady nature of massively separated flows and the ensuing wide, turbulent wake characteristic of deep stall conditions.

### 3.2 Flow-Field Visualization: Connecting Contours to Physics

### 3.2.1 Pressure and Velocity Distributions

The static pressure and velocity contours presented in Fig. 8 and Fig. 9 provide a direct spatial mapping of the flow physics governing performance. These visualizations align with fundamental principles: the region of highest velocity on the upper surface corresponds conclusively to the area of lowest static pressure, in accordance with Bernoulli’s theorem, and is the primary contributor to lift generation. Conversely, the prominent high-pressure zone at the leading-edge stagnation point is clearly captured.

### 3.2.2 Progression of Flow Separation Visualized

A phase-wise analysis of the contours reveals the physical progression toward stall:

- **Attached Flow Regime (e.g., 6°–8° AOA):** Contours show a thin, attached boundary layer and a strong, coherent low-pressure region extending over much of the upper surface. The adverse pressure gradient toward the trailing edge is mild, and flow separation is minimal or absent.

- **Incipient Stall Regime (~12°–14° AOA):** The adverse pressure gradient intensifies significantly. The velocity contours reveal a noticeable thickening of the boundary layer, and the low-pressure region on the aft upper surface begins to diminish and distort. This indicates the onset of trailing-edge separation, where near-wall flow reversal starts to erode the favorable pressure recovery.

- **Full Stall Regime (>16° AOA):** The separation point migrates rapidly upstream. The pressure contours exhibit a collapse of the suction peak, leading to a more uniform and higher pressure distribution over the entire upper surface. The velocity contours depict a large, recirculating wake region. This dramatic flow breakdown explains the precipitous drop in lift (stall) and the sharp rise in pressure drag.

### 3.3 Influence of Geometric Parameters on Flow Structures

### 3.3.1 Effect of Trailing-Edge Geometry

The comparison between sharp and square trailing edges reveals a distinct flow mechanism. The square trailing edge acts as a more potent flow separator. At high AOAs, it promotes earlier and more robust separation compared to the aerodynamically "clean" sharp edge. This is visualized in the contours as a more diffuse and upstream-displaced separation zone, resulting in a wider, more disordered wake. The consequent increase in form drag and reduction in circulation explain the observed degradation in peak $C_l/C𝑑$ and the earlier stall angle for square-edged profiles.

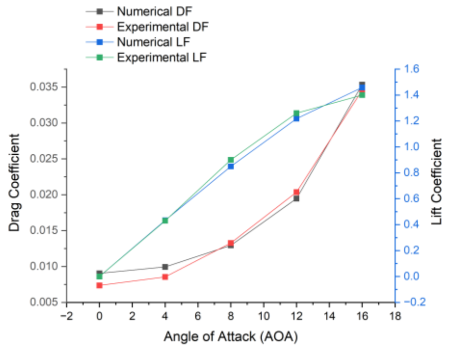

NACA Sharp Symmetry Profile

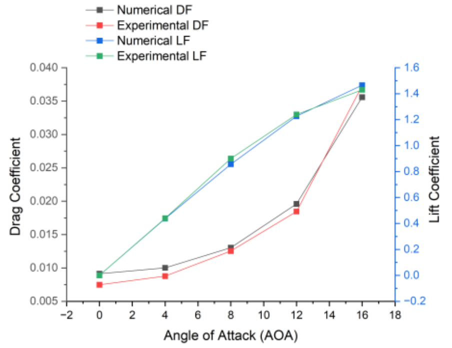

NACA Square Symmetry Profile

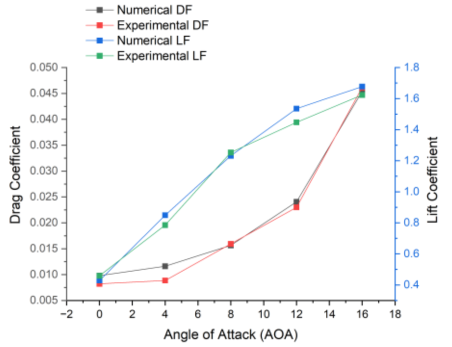

NACA Sharp Asymmetry Profile

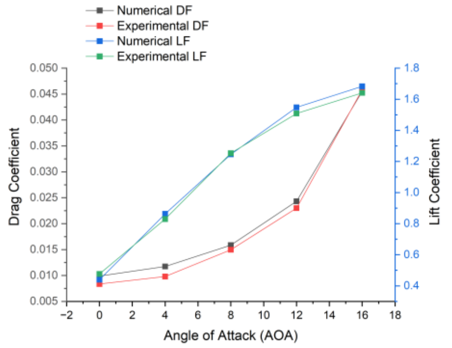

NACA Square Asymmetry Profile

Fig. 6 Coefficients vs Angle of Attack

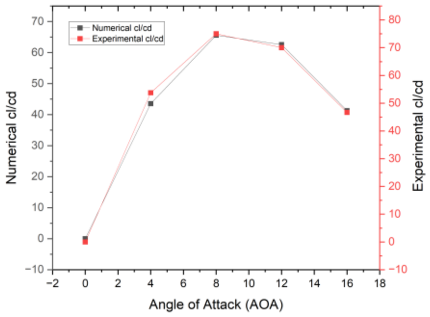

NACA Sharp Symmetry Profile

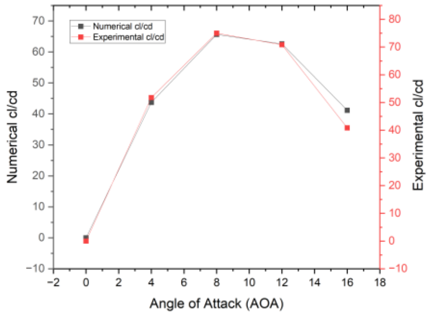

NACA Square Symmetry Profile

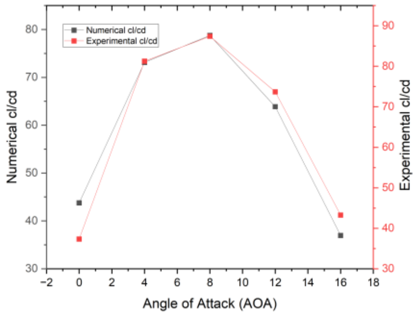

NACA Sharp Asymmetry Profile

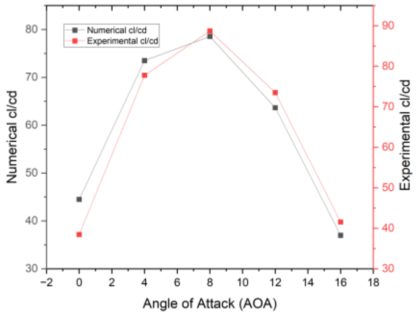

NACA Square Asymmetry Profile

Fig. 7 Cl/Cd vs Angle of attack

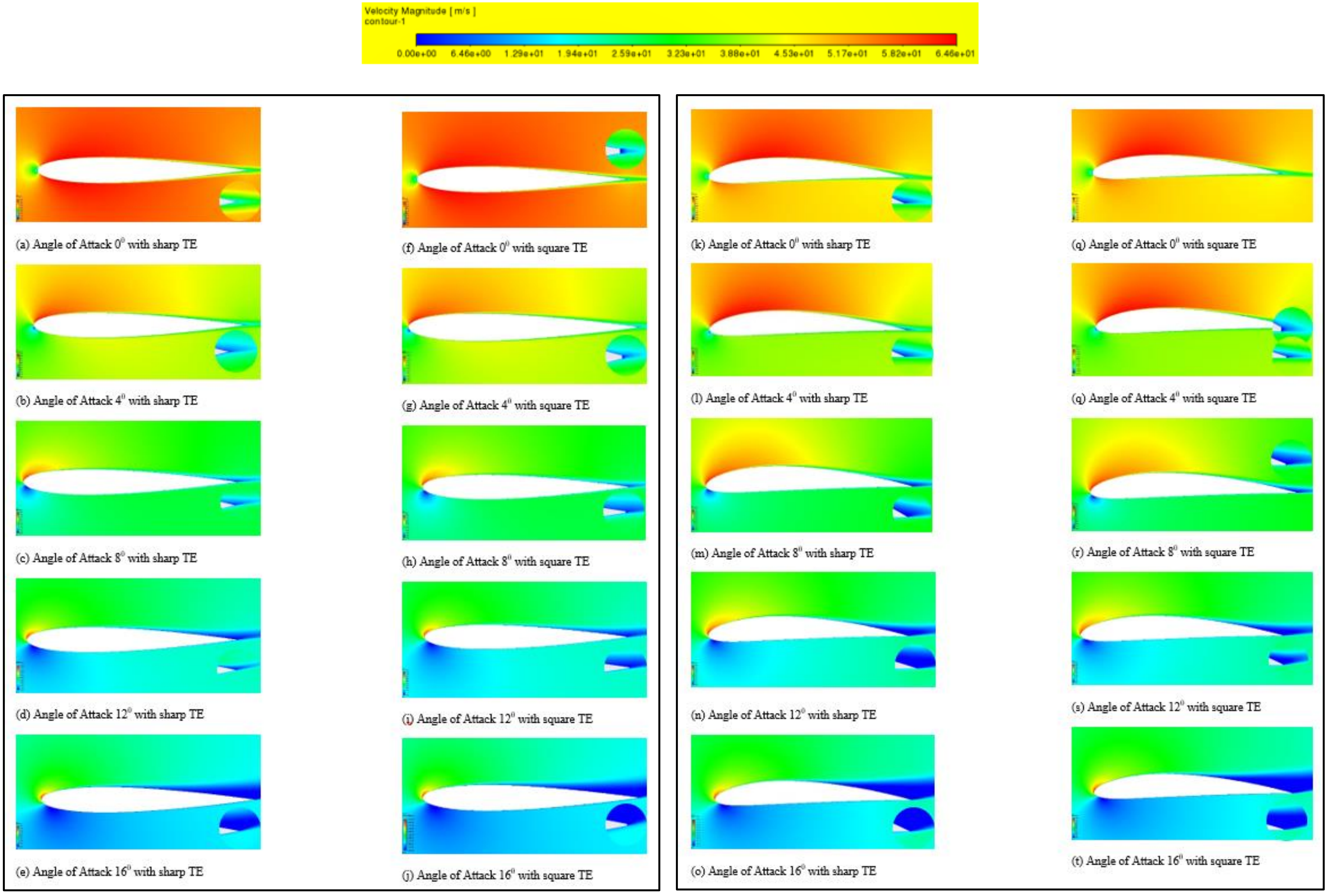

(a) Angle of Attack $0^{0}$ with sharp TE

(b) Angle of Attack $4^{0}$ with sharp TE

(c) Angle of Attack $8^{0}$ with sharp TE

(d) Angle of Attack $12^{0}$ with sharp TE

(e) Angle of Attack $16^{0}$ with sharp TE

(f) Angle of Attack $0^{0}$ with square TE

(g) Angle of Attack $4^{0}$ with square TE

(h) Angle of Attack $8^{0}$ with square TE

(i) Angle of Attack $12^{0}$ with square TE

(j) Angle of Attack $16^{0}$ with square TE

(k) Angle of Attack $0^{0}$ with sharp TE

(l) Angle of Attack $4^{0}$ with sharp TE

(m) Angle of Attack $8^{0}$ with sharp TE

(n) Angle of Attack $12^{0}$ with sharp TE

(o) Angle of Attack $16^{0}$ with sharp TE

(q) Angle of Attack $0^{0}$ with square TE

(q) Angle of Attack $4^{0}$ with square TE

(r) Angle of Attack $8^{0}$ with square TE

(s) Angle of Attack $12^{0}$ with square TE

(t) Angle of Attack $16^{0}$ with square TE

Fig. 8 Velocity Contour

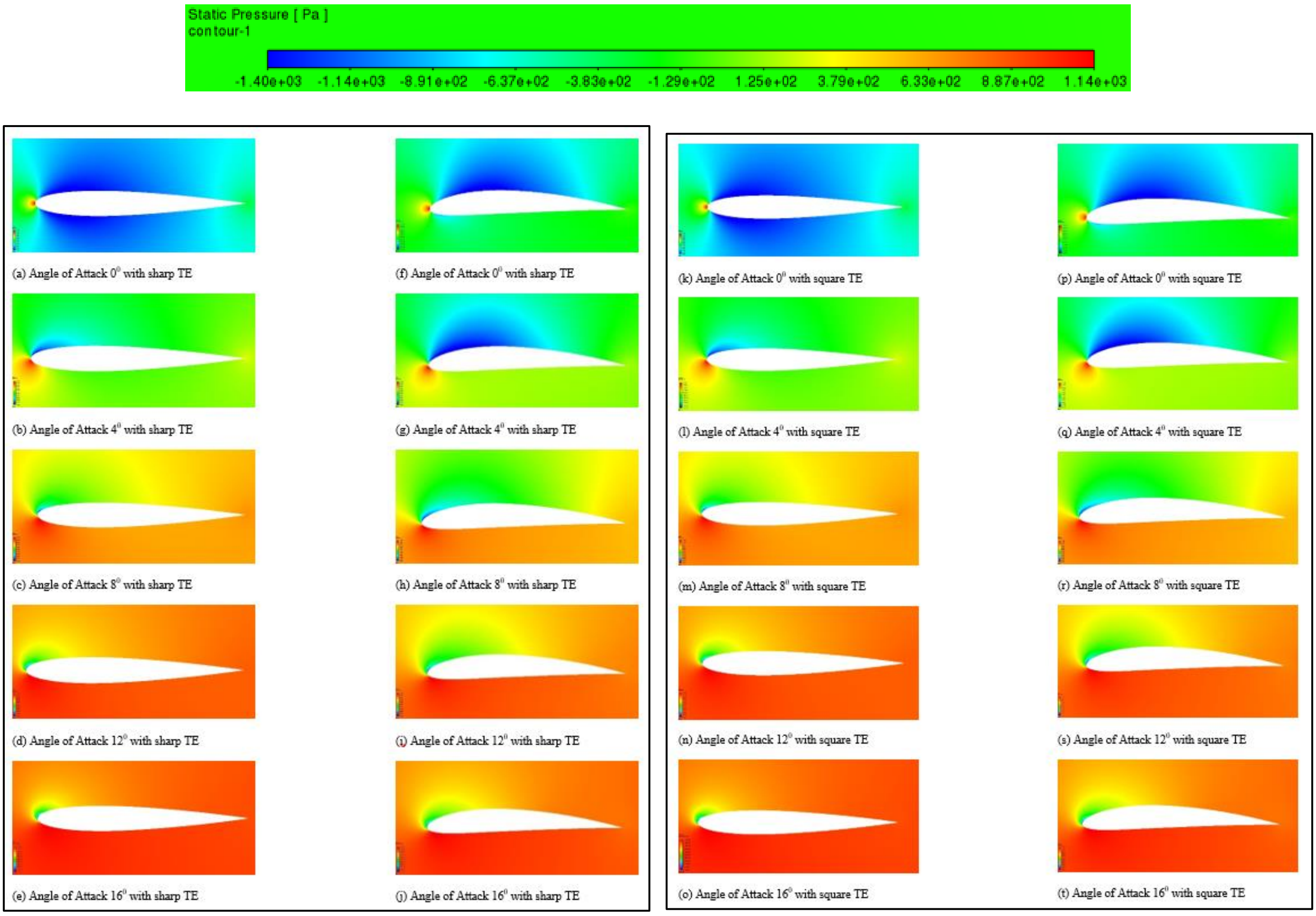

(a) Angle of Attack $0^{0}$ with sharp TE

(b) Angle of Attack $4^{0}$ with sharp TE

(c) Angle of Attack $8^{0}$ with sharp TE

(d) Angle of Attack $12^{0}$ with sharp TE

(e) Angle of Attack $16^{0}$ with sharp TE

(f) Angle of Attack $0^{0}$ with sharp TE

(g) Angle of Attack $4^{0}$ with sharp TE

(h) Angle of Attack $8^{0}$ with sharp TE

(i) Angle of Attack $12^{0}$ with sharp TE

(j) Angle of Attack $16^{0}$ with sharp TE

(k) Angle of Attack $0^{0}$ with square TE

(l) Angle of Attack $4^{0}$ with square TE

(m) Angle of Attack $8^{0}$ with square TE

(n) Angle of Attack $12^{0}$ with square TE

(o) Angle of Attack $16^{0}$ with square TE

(p) Angle of Attack $0^{0}$ with square TE

(q) Angle of Attack $4^{0}$ with square TE

(r) Angle of Attack $8^{0}$ with square TE

(s) Angle of Attack $12^{0}$ with square TE

(t) Angle of Attack $16^{0}$ with square TE

Fig. 9 Static Pressure Contour

### 3.3.2 Effect of Camber: Symmetric vs. Asymmetric Profiles

The inherent camber of asymmetric airfoils creates a non-zero pressure differential at zero AOA. The contours clearly show that, for a given AOA, the asymmetric airfoil maintains a more extensive and lower-pressure region on its upper surface compared to its symmetric counterpart. This geometry-induced pressure differential allows cambered airfoils to generate higher lift coefficients at lower angles of attack, thereby achieving a superior peak $C_l/Cd$. However, the analysis also shows that the stronger suction peak on cambered airfoils can sometimes lead to a more severe adverse pressure gradient on the aft section, potentially making them more susceptible to abrupt trailing-edge separation at high AOAs, as indicated by a more rapid post-peak decline in $C_l/Cd$ for some profiles.

### 3.4 Synthesis and Design Implications

In summary, this discussion moves beyond a descriptive presentation of results to provide a cause-and-effect analysis rooted in fluid dynamics. The quantitative performance metrics ($C_l$, $Cd$, $C_l/Cd$) are explicitly linked to the evolution of physical flow structures—namely, the development of the leading-edge suction peak, the intensification of the adverse pressure gradient, the initiation and forward progression of boundary-layer separation, and the consequent formation of a low-energy wake. The systematic comparison of geometries demonstrates that while global parameters like AOA dominate the performance envelope, local features such as trailing-edge shape and camber distribution critically modulate the flow separation dynamics, thereby defining the precise stall characteristics and efficiency plateau for a given design. The identified discrepancy between simulation and experiment at high AOAs highlights a critical area for future CFD model development, specifically in improving the prediction of post-stall, massively separated flows. These findings underscore the necessity of a holistic design approach that considers not only the target lift coefficient but also the detailed pressure gradient management and separation control dictated by the intended operational AOA range.

## 4 Conclusion

In conclusion, this CFD-based investigation demonstrates that while the angle of attack is the predominant factor governing airfoil performance, the interaction between camber and trailing-edge geometry presents a significant opportunity for targeted aerodynamic optimization. The observed peak lift-to-drag ratio at 8° angle of attack, along with the more rapid performance degradation of asymmetric airfoils, underscores the nuanced interdependence of these geometric parameters. Furthermore, the finding that trailing-edge efficacy is contingent on the base airfoil profile highlights the necessity for a holistic design approach. Ultimately, this study confirms that tailoring camber and trailing-edge configuration to specific operational requirements is essential for advancing airfoil performance, providing a foundation for future aerodynamic optimization.

## Acknowledgements

The author is thankful to Xi’an Jiaotong University, China and other supporting institutes for providing the opportunity to finish this research work.

## Author Contributions

**M. Shahryar**: Data Curation, Formal Analysis, Investigation, Resources, Software, Validation, Visualization, Writing – Original Draft; **M. Fahadyar**: Conceptualization, Methodology, Project administration, Supervision, ,Writing – Review & Editing.

## Conflicts of Interest

The authors declare no conflicts of interest.

## Funding Information

This research did not receive any specific grant from funding agencies in the public, commercial, or not-for-profit sectors.

## Generative Artificial Intelligence Statement

While preparing this work, the authors used ChatGPT to improve the writing quality of some paragraphs. They confirm that no generative artificial intelligence (Gen AI) was used in creating this manuscript.

## Data Availability

All data generated or analyzed during this study are included in this published article.

## Nomenclature

| | |
|---|---|
| $C_d$ | Drag Coefficient |
| $C_l$ | Lift Coefficient |
| $C_p$ | Pressure Coefficient |
| L | Chord Length |
| p | Pressure |
| $v$ | kinematic viscosity |
| $v_T$ | Eddy viscosity |
| $\rho$ | Density |
| $\rho_\infty$ | Free-stream density |
| $p$ | local static pressure |
| $F_d$ | Drag force |
| $F_l$ | Lift force |
| AoA | Angle of attack |
| TE | Trailing Edge |

## References

[1] Glauert, H. (1929). Glauert_the_elements_of_airfoil_ and_ airscrew_theory.

[2] Kanimozhi, V. G. (2018). Analysis of Airfoil Flow Pattern using CFD. International Journal of Engineering Research & Technology, 6(14), 1–5.

[3] GÖRGÜLÜ, Y. F., ÖZGÜR, M. A., & KÖSE, R. (2021). CFD Analysis of a Naca 0009 Aerofoil at a Low Reynolds Number. *Politeknik Dergisi*, *24*(3), 1237–1242.

[4] Chumbre, V., Rushikesh, T., Umatar, S., & Kerur, S. M. (2018). CFD Analysis of Airfoil Sections. International Research Journal of Engineering and Technology (IRJET), 5(7), 349–353.

[5] Peng, Z., Chen, B., Qin, F. G. F., Jiang, R., He, Q., Tao, S., Xiao, H., Chen, Y., & Yang, M. (2019). Numerical simulation of aerodynamic performance of an airfoil combined lift and drag. Energy Procedia, 158, 6282–6287.

[6] Rabei, I. (2021). Vertical Axis Wind Turbines: Open Airfoils and Plastic Blades. SIELMEN 2021 - Proceedings of the 11th International Conference on Electromechanical and Energy Systems, 51–56.

[7] Rabei, I. (2021). Vertical Axis Wind Turbines: Open Airfoils and Plastic Blades. SIELMEN 2021 -

Proceedings of the 11th International Conference on Electromechanical and Energy Systems, 51–56.

[8] Rama Rao, Y. S., Srujan Manohar, M. V. N., & Siva Praveen, S. V. V. (2021). CFD simulation of NACA airfoilsat various angles of attack. IOP Conference Series: Materials Science and Engineering, 1168(1), 012011.

[9] Zhao, Z., Wang, D., Wang, T., Shen, W., Liu, H., & Chen, M. (2022). A review: Approaches for aerodynamic performance improvement of lift-type vertical axis wind turbine. Sustainable Energy Technologies and Assessments, 49, 101789

[10] Islam Rubel, R., Kamal Uddin, M., Zahidul Islam, M., & Rokunuzzaman, M. (2017). Numerical and Experimental Investigation of Aerodynamics Characteristics of NACA 0015 Aerofoil. International Journal of Engineering Technologies IJET, 2(4), 132–141.

[11] Aqilah, F., Islam, M., Juretic, F., Guerrero, J., Wood, D., & Ani, F. N. (2018). Study of mesh quality improvement for CFD analysis of an airfoil. IIUM Engineering Journal, 19(2), 203–212.

[12] Wolfe, W., & Ochs, S. (1997). Predicting Aerodynamic Characteristics of Typical Wind Turbine Airfoils Using CFD. Sandia Repo, September, 25–30.

[13] Langtry, R. B., Gola, J., & Menter, F. R. (2006). Predicting 2D airfoil and 3D wind turbine rotor performance using a transition model for general CFD codes. Collection of Technical Papers - 44th AIAA Aerospace Sciences Meeting, 7, 4643–4653.

[14] Dr.Abhishek. (2021). (PDF) Basics of Aerofoil simulation.

[15] Wilcox, D. C. (2008). Formulation of the k-ω turbulence model revisited. AIAA Journal, 46(11), 2823–2838.